

Theoretical Study of Rotary Freestanding Triboelectric Nanogenerators

Tao Jiang, Xiangyu Chen, Chang Bao Han, Wei Tang, and Zhong Lin Wang*

The use of triboelectric nanogenerators (TENG) is a highly effective technology for harvesting ambient mechanical energy to produce electricity. In this work, a theoretical model of rotary freestanding TENG with grating structure is constructed, including the conductor-to-dielectric and dielectric-to-dielectric categories. The finite element simulations are performed to capture the fundamental physics of rotary freestanding TENG. Based on the simulations and derivations of approximate analytical equations, the real-time output characteristics of TENG with arbitrary load resistance are calculated. Furthermore, the influences of structural parameters of TENG and rotation rate on the output performance are investigated. The theory presented here facilitates a deep understanding of the working mechanism of rotary freestanding TENG and provides useful guidance for designing high performance TENG for energy harvesting applications.

1. Introduction

Harvesting energy from our natural environment has attracted extensive interests due to the increasing demands on worldwide energy supply.^[1–3] Mechanical energy, as a universally available and sustainable resource, has been primarily scavenged through diverse approaches based on piezoelectric effect,^[4,5] electrostatic effect,^[6] and thermoelectric effect,^[7] etc. Recently, triboelectric nanogenerator (TENG) has emerged as a powerful technology for harvesting mechanical energy, with advantages of high output power, high efficiency, low fabrication cost, and no pollution.^[8–13] The TENG can convert mechanical energy to electricity through the coupling effect of contact electrification and electrostatic induction.^[14–16] Compared with two basic modes of TENG, i.e., sliding-mode^[17] and contact-mode,^[18,19] it is not necessary to attach the moving triboelectric layer with an electrode and a lead wire for freestanding TENG, therefore this TENG presents advantageous in harvesting mechanical energies from an arbitrary moving object or a walking human.^[20–22] Rotary freestanding TENG (RF-TENG)

with microsized grating disk-structure and radial-arrayed complementary electrodes has been demonstrated experimentally to possess unprecedentedly high performance.^[23–26] However, there still lacks a theoretical model to systematically provide an in-depth understanding of its working principle. In addition, the impacts of structural parameters and operation conditions of RF-TENG on the output performance, which are critical for characteristic optimization, are still unclear enough.

In the present work, a comprehensive theoretical model was built for the rotary freestanding TENG with a grating structure. The fundamental physics of RF-TENG was revealed by the finite element method (FEM), in which the influences

of grating number and electrode gap were addressed. Based on the FEM results, an approximate analytical governing equation was constructed, and the dynamic output characteristics of TENG were mathematically calculated for both conductor-to-dielectric and dielectric-to-dielectric types. Finally, we investigated the effects of structural parameters and rotation rate on the output power and optimum resistance.

2. Conductor-to-Dielectric Rotary Freestanding TENG

A rotary freestanding TENG consisting of a stator and a rotator can have many types due to the diversity design of triboelectric materials and their structures. We mainly focused on the TENGs designed based on the triboelectrification between metal or dielectric layer of rotator and dielectric layer of stator, i.e., conductor-to-dielectric and dielectric-to-dielectric categories. We first take the conductor-to-dielectric category as an example. The FEM model for this type of TENG (metal RF-TENG) with a grating structure was constructed as shown in Figure 1a. A 3D model was utilized, in which the dimensions are close to those of real devices. In the stator part, complementary A and B metal electrodes with a thickness of 0.01 mm are attached by a dielectric layer (a thickness of 0.05 mm, represented by d) with the same grating. The gap angle between each A and B metal unit and the center angle of grating unit are defined as θ_g and θ_0 , respectively. A metal freestanding layer with the same size and grating as Electrode A stands on the top surface of dielectrics. The freestanding layer with the thickness of 0.01 mm can rotate clockwise around the central axis of TENG (the rotation angle is represented by α). The number of

Dr. T. Jiang, Prof. X. Chen, Dr. C. B. Han, Dr. W. Tang,
Prof. Z. L. Wang
Beijing Institute of Nanoenergy and Nanosystems
Chinese Academy of Sciences
Beijing 100083, China
E-mail: zlwang@gatech.edu

Prof. Z. L. Wang
School of Materials Science and Engineering
Georgia Institute of Technology
Atlanta, GA 30332-0245, USA

DOI: 10.1002/adfm.201500447



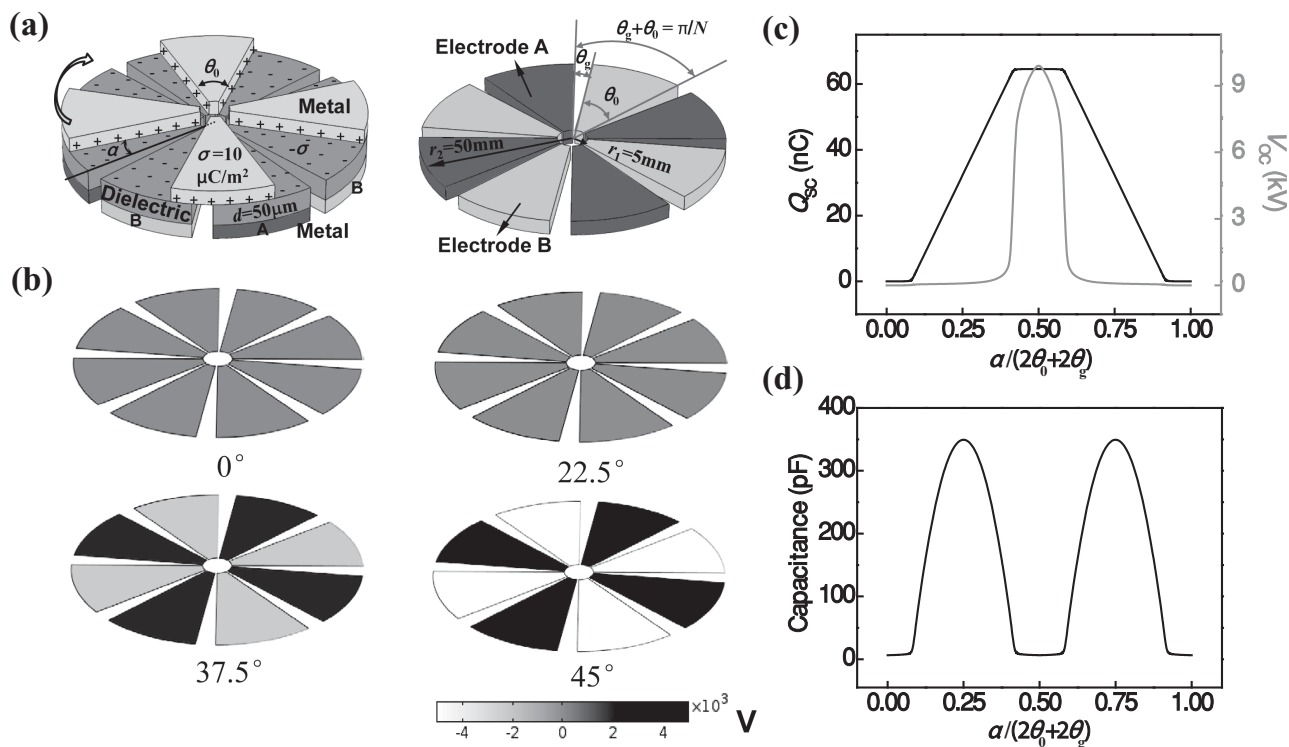


Figure 1. a) FEM model of metal rotary freestanding TENG. The complementary electrode structure is also shown. b) Electric potential distributions on the electrodes under the reference state for $N = 4$ and $\theta_g/\theta_0 = 1/5$. c) Short-circuit charge and open-circuit voltage as functions of rotation angle during one full cycle under the reference state. d) Capacitance versus rotation angle.

grating units in the freestanding layer is defined as N , and the inner and outer radius of TENG (denoted by r_1 and r_2) are fixed as 5 and 50 mm. (Detailed calculation parameters are listed in Table 1.) Due to contact electrification, different signs of static charges (called tribo-charges) are distributed at the freestanding metal and the upper surface of dielectrics. We assume that the negative tribo-charges are uniformly distributed on the dielectric surface with a density of $-\sigma$. For charge conservation, the freestanding metal will have the same amount of positive charges in total.

It is noted that the influence of contact force between triboelectric surfaces (tribo-surfaces) was not considered in this work. Compared with the influences of rotation angle and rate on the electrical output performance, the influence of contact force is rather complicated. Generally speaking, the surface charge density (σ) in the steady state depends on the material properties (e.g., work function difference, dielectric constant, etc.)

Table 1. Parameters utilized in the FEM calculation for metal RF-TENG.

| | |
|--|-------------------------------------|
| Dielectric | $\epsilon_r = 3, d = 50 \text{ mm}$ |
| Inner radius r_1 of TENG | 5 mm |
| Outer radius r_2 of TENG | 50 mm |
| Tribo-charge surface density σ | $10 \mu\text{C m}^{-2}$ |
| Grating number N | 1–8 |
| Center angle of grating unit θ_0 , gap angle θ_g | $\theta_0 + \theta_g = \pi/N$ |
| Angle velocity ω of rotation | $20\pi \text{ rad s}^{-1}$ |

of two contacted materials, which is independent of applied contact force.^[27,28] However, if the contact force is lower than a threshold value, the incomplete contact between two surfaces results in the decrease of saturated surface charge density. Meanwhile, it is much difficult to get some quantitative analysis between the contact force and the contact completeness due to the variability of surface morphology and experimental repeatability. Therefore, to simplify the numerical calculations, we assume that the contact between two tribo-surfaces is perfect and thereby the contribution from contact force is negligible. On the other hand, the tribo-charges need to experience several rotation cycles until they can reach their saturated values. The contact force may accelerate this process, leading to different output performances of TENG in the first few cycles. Nevertheless, finally, the steady-state output performance is still independent of the applied contact force.

The FEM calculations under the short-circuit (SC) and open-circuit (OC) conditions were carried out utilizing the COMSOL software. The metal units in each electrode group were assigned with the same electric potential to reflect the external connection. At the initial state, the freestanding metal layer is placed to match with Electrode A. The total charge on Electrode A is $Q + Q_{\text{initial}}$ and that on Electrode B is $-Q - Q_{\text{initial}}$, in which Q_{initial} is the equilibrium charge level at the initial state and Q is the amount of transferred charges at a certain rotation angle α . Q_{initial} was assigned to the total amount of charges transferred at $\alpha = 0$ under SC condition. The SC transferred charges (Q_{SC}) was calculated by deducting Q_{initial} from total transferred charges under SC ($Q_{\text{net,SC}}$) at a certain angle α . The

charge reference state (SC state at $\alpha = 0$) was chosen to facilitate the theoretic calculations, similar to our previous work.^[29] Then the OC voltage (V_{OC} , voltage at $Q = 0$) for various α was obtained by assigning the total charges of Electrode A and Electrode B to Q_{initial} and $-Q_{\text{initial}}$. The total capacitance, which is an inherent character of TENG and independent of the reference state, was extracted by the interpolation method based on the $V-Q-\alpha$ relationship.^[30,31]

Typical electric potential distributions on the electrodes with variable rotation angles under the reference state when setting $N = 4$ and $\theta_g/\theta_0 = 1/5$ are shown in Figure 1b. The results of half cycle show no electric potential difference between the two electrodes at $\alpha = 0$, as expected. When the freestanding metal rotates to the middle position ($\alpha = (\theta_0 + \theta_g)/2$, 22.5°), the potential difference is still very small. When the freestanding layer approaches the matched region of Electrode B ($\alpha = \theta_0 + \theta_g$, 45°), a maximum potential difference of ≈ 10 kV is generated, and the V_{OC} starts increasing drastically at $\alpha = \theta_0$ (Figure 1c). The sharp increase in V_{OC} is ascribed to the quick drop of capacitance (Figure 1d). The capacitance exhibits a bimodal feature during one full cycle, and has the maxima at the middle positions ($\alpha = (\theta_0 + \theta_g)/2$, $3(\theta_0 + \theta_g)/2$). The Q_{SC} curve during one full cycle indicates that the Q_{SC} nearly keeps constant at the angle ranges of $0 \leq \alpha \leq \theta_g$, $\theta_0 \leq \alpha \leq \theta_0 + 2\theta_g$, and $2\theta_0 + \theta_g \leq \alpha \leq 2\theta_0 + 2\theta_g$. However, it increases linearly with the rotation angle at $\theta_g \leq \alpha \leq \theta_0$ and decreases linearly at $\theta_0 + 2\theta_g \leq \alpha \leq 2\theta_0 + \theta_g$. The simulation results of Q_{SC} are in accordance with the following theoretical $Q_{SC}-\alpha$ equation derived based on ideal charge distribution under SC condition and electrostatic equilibrium. (For a detailed derivation, see the Supporting Information, Section 1.)

$$Q_{SC} = 0, \quad 0 \leq \alpha \leq \theta_g, \quad \text{and} \quad 2\theta_0 + \theta_g \leq \alpha \leq 2\theta_0 + 2\theta_g \quad (1a)$$

$$Q_{SC} = \frac{N\theta_0\sigma(\alpha - \theta_g)(r_2^2 - r_1^2)}{\theta_0 - \theta_g}, \quad \theta_g \leq \alpha \leq \theta_0 \quad (1b)$$

$$Q_{SC} = N\theta_0\sigma(r_2^2 - r_1^2), \quad \theta_0 \leq \alpha \leq \theta_0 + 2\theta_g \quad (1c)$$

$$Q_{SC} = \frac{N\theta_0\sigma(2\theta_0 + \theta_g - \alpha)(r_2^2 - r_1^2)}{\theta_0 - \theta_g}, \quad \theta_0 + 2\theta_g \leq \alpha \leq 2\theta_0 + \theta_g \quad (1d)$$

Note that the rotating-induced transferred charge change under the SC condition barely depends on the choice of charge reference state, however, the V_{OC} curve is greatly affected (Figure S5, Supporting Information, real electric potential distribution, short-circuit charge, and open-circuit voltage).

The gap angle between two electrodes is an important design parameter of the RF-TENG, which may affect the basic properties of TENG. Due to the unique character of grafting disk structure, the relative ratio of gap angle to the center angle of grating unit (θ_g/θ_0) was adopted to reflect the gap effect. The influences of θ_g/θ_0 ratio on the short-circuit charge (Q_{SC}), capacitance (C), open-circuit voltage (V_{OC}), and short-circuit current (I_{SC}) for $N = 4$ were studied, as shown in Figure 2. It can be seen that Q_{SC} , C , and V_{OC} all have mirror symmetry in one cycle for assigned θ_g/θ_0 ratios. The Q_{SC} in a half cycle ($T/2$) has two constant regions and a middle linear region, and reaches its maximum $Q_{SC-\text{max}}$ at the $T/2$ point, where the $Q_{SC-\text{max}}$ decreases with

the increase of θ_g/θ_0 ratio due to the decrease of tribo-surface area (Figure 2a). However, the Q_{SC} curve exhibits a higher slope in the linear region for a larger θ_g/θ_0 , specifically, for $\theta_g/\theta_0 = 1/1$, the Q_{SC} sharply increases at $T/4$ (full nonmatched between top metal and Electrode A). The total capacitance C , which contains the parasitic capacitance C_p between electrodes and the serial connection of capacitance between top metal and Electrode A (C_A) and between top metal and Electrode B (C_B), was also found to decrease with the increase of θ_g/θ_0 (Figure 2b). Extremely, when $\theta_g/\theta_0 = 1/1$, the C is nearly constant with the change of rotation angle, because the top metals only have overlapping region with dielectric units on top of one electrode ($C_A = 0$ or $C_B = 0$). Note that for any θ_g/θ_0 , at the zero and $T/2$ points (when top metal is matched with Electrode A or B), the capacitance C approximately equals the C_p between electrodes, so the C_p decreases (from 8.705 to 3.756 pF) with increasing the θ_g/θ_0 ratio (from $1/14$ to $1/1$). The maximum value ($V_{OC-\text{max}}$) of V_{OC} first increases as the θ_g/θ_0 ratio increases, and then decreases at larger θ_g/θ_0 (Figure 2c), which may be ascribed to the competition between the decreasing speed of Q_{SC} and C .

Based on the FEM results, we can also calculate short-circuit current I_{SC} of the metal RF-TENG with an assumed specific motion mode. When the freestanding metals are assumed to rotate at a constant angle velocity ω (20π rad s^{-1}), the I_{SC} curves were obtained through the differentiation of Q_{SC} data in Figure 2a. As expected, the I_{SC} has a constant value in the middle linear region except for $\theta_g/\theta_0 = 1/1$, which can be enhanced by the increase in θ_g/θ_0 (Figure 2d). The numerically calculated results are consistent with the theoretical formula of I_{SC} derived from Equations (1a)–(1d), given by

$$I_{SC} = \frac{N\theta_0\sigma(r_2^2 - r_1^2)}{\theta_0 - \theta_g} \times \frac{d\alpha}{dt}, \quad \theta_g \leq \alpha \leq \theta_0 \quad (2a)$$

$$I_{SC} = -\frac{N\theta_0\sigma(r_2^2 - r_1^2)}{\theta_0 - \theta_g} \times \frac{d\alpha}{dt}, \quad \theta_0 + 2\theta_g \leq \alpha \leq 2\theta_0 + \theta_g \quad (2b)$$

$$I_{SC} = 0, \quad \text{else} \quad (2c)$$

The equation is not suited for the special case of $\theta_g/\theta_0 = 1/1$, in which two high acute peaks emerge at $T/4$ and $3T/4$ in the I_{SC} curve.

Besides the electrode gap, the grating number N is another important structural parameter having direct impacts on the output properties of TENG. When N starts to increase from 1, the approximate ideal charge distribution is still satisfied because the geometric size of grating unit (arc length l of each unit) is still much larger than the thickness d of dielectrics. However, when N is increased to fairly large values and l is comparable with d , the nonideal edge effect is significant and cannot be neglected any longer. The influence of N in relatively small regions under ideal conditions can be learned from Equations (1a)–(1d) and (2a)–(2c). The charge transfer efficiency under SC condition (η_{SC} , defined as the ratio of Q_{SC} to total tribo-charge amount Q_{tribo}) can reach 100% at the half-cycle $T/2$. Based on the $Q_{SC}-N$ relationship, we can also calculate the accumulated charges ($Q_{SC-\text{rectified}}$) and charge transfer efficiency ($\eta_{SC-\text{rectified}}$) after rectification under SC when a rotation angle of π is finished by the following equations

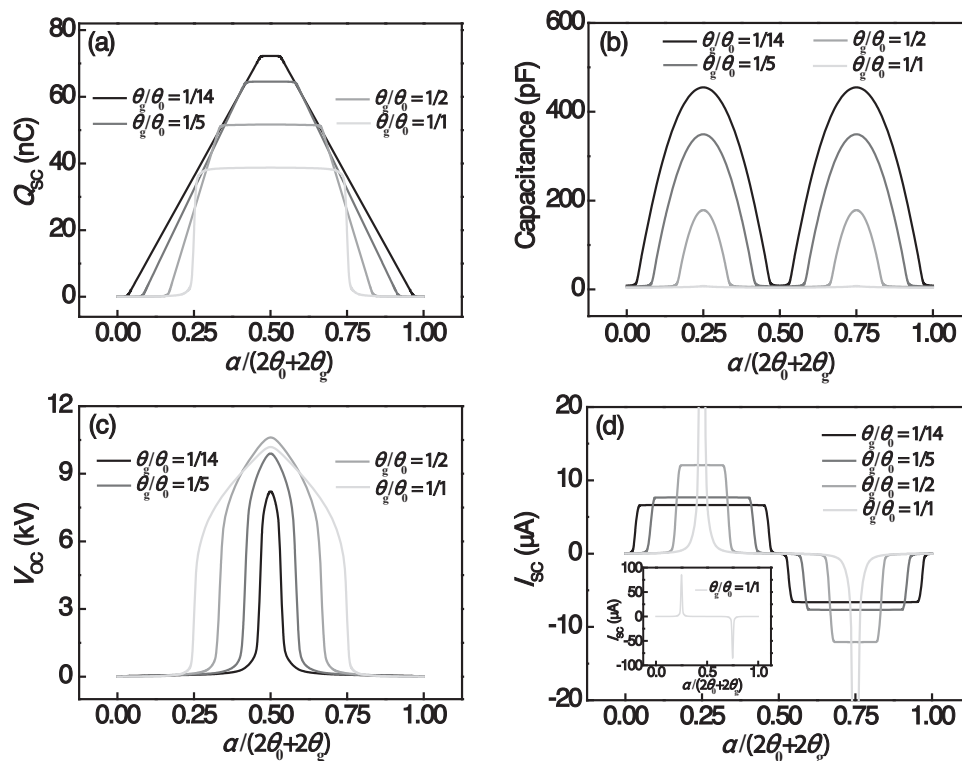


Figure 2. a) Short-circuit charge Q_{SC} , b) capacitance C , c) open-circuit voltage V_{OC} , and d) short-circuit current I_{SC} of metal RF-TENG ($N = 4$) during one full cycle for various θ_g/θ_0 ratios under the reference state. In d), the inset shows the complete I_{SC} curve for $\theta_g/\theta_0 = 1/1$.

$$Q_{SC\text{-rectified}}(\alpha = \pi) = N^2 \theta_0 \sigma (r_2^2 - r_1^2) = \frac{N \pi \sigma (r_2^2 - r_1^2)}{1 + \theta_g / \theta_0} \quad (3)$$

$$\eta_{SC\text{-rectified}}(\alpha = \pi) = \frac{Q_{SC\text{-rectified}}(\alpha = \pi)}{Q_{\text{tribo}}} = N \quad (4)$$

From above equations, it can be seen that the saturated value of I_{SC} , $Q_{SC\text{-rectified}}$, and $\eta_{SC\text{-rectified}}$ in the grating-disk structure can be enhanced by N times through the subdivision process under ideal conditions for a fixed θ_g/θ_0 ratio. Note that the $\eta_{SC\text{-rectified}}$ can exceed 100% due to the multiple cycles of charge separation.

In order to validate the theoretic analysis, FEM simulations were performed for the grating-structured metal RF-TENG under ideal conditions ($L/d = 628.3$, L denotes the circumference of inner circle, detailed calculation parameters are the same as shown in Table 1). The results of Q_{SC} , I_{SC} , C , and V_{OC} for a fixed θ_g/θ_0 (1/5) are presented in Figure 3a–d. The numerically calculated results are in good agreement with the theoretic equations. As the grating number N increases from 1 to 8, Q_{SC} remains almost the same in each cycle, but the increase of cycle number for a given rotation angle significantly elevates the amount of accumulated charges after rectification (Figure 3a). The I_{SC} increases with N because of the decrease of period T (Figure 3b). However, for the open-circuit voltage, the $V_{OC\text{-max}}$ at larger N significantly drops (Figure 3d), since a finer pitch leads to an increase in capacitance when the top metal is matched with Electrode B (Figure 3c).

As the grating number N increases, the gaps between electrodes become narrower, which leads to the increase of parasitic capacitance C_p between electrodes. The serial capacitance of C_A and C_B is almost unaffected by the N , because the overlapped region area between top metal and dielectric units cannot be changed by N for a given θ_g/θ_0 ratio. Therefore, the total capacitance C increases with increasing the N value. As shown in Figure 3a,c, the TENG exhibits a very low C close to C_p and a high nearly-saturated Q_{SC} at $\theta_0 \leq \alpha \leq \theta_0 + \theta_g$. When the top metal is matched with Electrode B, the capacitance reaches its minimum value C_p , while the Q_{SC} reaches its maximum value. Because the C_p increases from 3.67 to 13.857 pF (by 3–4 times) with increasing N from 1 to 8, the V_{OC} (obtained from $V_{OC} = Q_{SC}/C$) increases significantly with N . The marked change in capacitance with N can be viewed from the inset of Figure 3c.

When N increases to very large values (l/d is very small), the nonideal edge effect cannot be neglected, so those above theoretic equations will not be appropriate. To investigate the influence of the nonideal effect, we calculated the Q_{SC} and η_{SC} for a grating RF-TENG with a small L/d ratio of 12.6 ($r_1 = 0.1$ mm, $r_2 = 0.2$ mm, and $d = 0.05$ mm) at $\theta_g/\theta_0 = 1/5$ in one cycle, as shown in Figure 3e. It indicates that the maximum values of Q_{SC} and η_{SC} in each period both descend markedly with the increase of N . The maximum η_{SC} decreases from 67.7% to 11.4% as the N increases from 1 to 8, where the charge transfer efficiency becomes far from the theoretical value of 100% due to the nonideal effect. That results in the emerging of maximum $Q_{SC\text{-rectified}}$ and $\eta_{SC\text{-rectified}}$ at a low optimum grating number ($N = 4$, Figure 3f), which may guide the structural design of

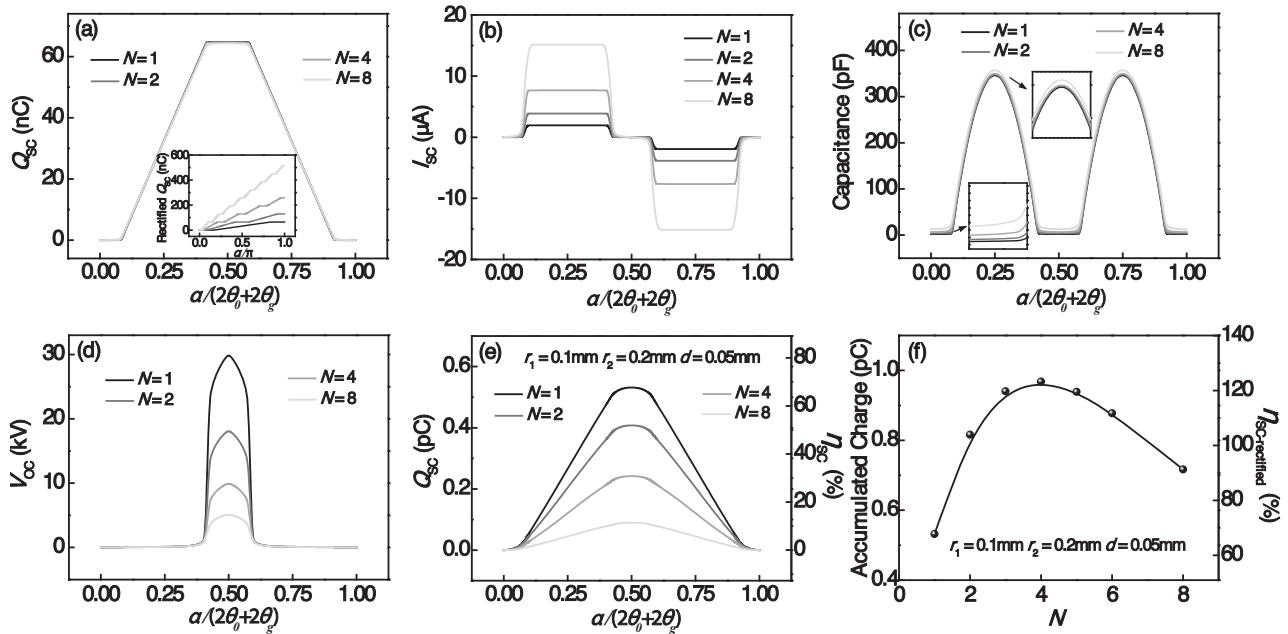


Figure 3. a) Short-circuit charge, b) short-circuit current, c) capacitance, and d) open-circuit voltage of metal RF-TENG during one cycle for various grating numbers under the reference state. e) Q_{SC} and η_{SC} profiles of TENG with a small L/d ratio during one cycle at different N . f) Total SC transferred charge and efficiency with respect to N when rotating for the angle of π .

the grating RF-TENG to obtain the optimum charge for specific applications.

To better understand the fundamental physics and output characteristics of the metal RF-TENG, it is important to provide analytical equations for the three basic property qualities of Q_{SC} , C , and V_{OC} , maybe utilizing some approximates. For a certain electrode gap (θ_g/θ_0), the ideal Q_{SC} - α relationship of the TENGs can be found in Equations (1a)–(1d). However, there are no appropriate analytical equations for the capacitance and open-circuit voltage due to the edge effect. In the region at $\theta_0 \leq \alpha \leq \theta_0 + \theta_g$, the capacitance drops to a very low value close to the capacitance C_p between electrodes because the top metals move to only overlap with the top dielectrics of Electrode B ($C_A \approx 0$). The capacitance has a very slight decrease so that it can be considered unchanged relative to the maximum capacitance. But the V_{OC} exhibits a sharp rise in this region, which is contributed from the high Q_{SC} and the relation $V_{OC} = Q_{SC}/C$. In this respect, the slight change of C including gap edge effect cannot be neglected. If the electrode gap is depressed to the degree at which it can be neglected (the sharp rising region of V_{OC} can be significantly cut down), the edge effect may be eliminated approximately. Meanwhile, a smaller electrode gap leads to higher SC transferred charge and tribo-charge amounts for designed TENGs due to the larger tribo-surface area (Figure 2a). The maximization of transferred charges and tribo-charges of TENG is necessary for specific practical applications such as charging a battery or a capacitor. Based on these considerations, the consequent resistive load characteristics of metal RF-TENG were calculated mathematically focusing on the case of neglecting the electrode gap.

When neglecting the electrode gap, the ideal equation of Q_{SC} (Equations (1a)–(1d)) can be transformed into the following equation

$$Q_{SC} = \begin{cases} N\sigma\alpha(r_2^2 - r_1^2) & 0 \leq \alpha \leq \theta_0 \\ N\sigma(2\theta_0 - \alpha)(r_2^2 - r_1^2) & \theta_0 \leq \alpha \leq 2\theta_0 \end{cases} \quad (5)$$

Then the total capacitance C composed of C_A , C_B , and C_p is deducted. According to the parallel-plate capacitor model, the capacitance C can be estimated by the following equation:

$$C = \begin{cases} \frac{N\epsilon_0\epsilon_r\alpha(\theta_0 - \alpha)(r_2^2 - r_1^2)}{2d\theta_0} + C_p & 0 \leq \alpha \leq \theta_0 \\ \frac{N\epsilon_0\epsilon_r(\alpha - \theta_0)(2\theta_0 - \alpha)(r_2^2 - r_1^2)}{2d\theta_0} + C_p & \theta_0 \leq \alpha \leq 2\theta_0 \end{cases} \quad (6)$$

where ϵ_0 and ϵ_r represent the permittivity of vacuum and relative permittivity of dielectrics. For details, see Section 3 in the Supporting Information. It is noted that when one of two overlapped regions between top metal and dielectrics is very narrow, this approximate equation is still available although the edge effect exists, since the capacitance component in the narrow overlapped region makes slight contribution to the total capacitance. The V_{OC} will be obtained from the Q_{SC} divided by C . These theoretical equations were found to match the FEM results quite well (Figure S7, Supporting Information). Therefore, the governing equation of metal RF-TENG, i.e., V - Q - α relationship

$$V = -\frac{1}{C(\alpha)} \times Q + V_{oc}(\alpha) \quad (7)$$

can be approximately written as

$$V = -\frac{2d\theta_0}{N\epsilon_0\epsilon_r\alpha(\theta_0 - \alpha)(r_2^2 - r_1^2) + 2d\theta_0C_p} Q + \frac{2Nd\theta_0\sigma\alpha(r_2^2 - r_1^2)}{N\epsilon_0\epsilon_r\alpha(\theta_0 - \alpha)(r_2^2 - r_1^2) + 2d\theta_0C_p}, \quad 0 \leq \alpha \leq \theta_0 \quad (8a)$$

$$V = -\frac{2d\theta_0}{N\epsilon_0\epsilon_r(\alpha - \theta_0)(2\theta_0 - \alpha)(r_2^2 - r_1^2) + 2d\theta_0C_p} Q + \frac{2Nd\theta_0\sigma(2\theta_0 - \alpha)(r_2^2 - r_1^2)}{N\epsilon_0\epsilon_r(\alpha - \theta_0)(2\theta_0 - \alpha)(r_2^2 - r_1^2) + 2d\theta_0C_p}, \quad \theta_0 \leq \alpha \leq 2\theta_0 \quad (8b)$$

The load characteristics can be calculated by combining the analytical V - Q - α relationship and Ohm's law through the following equation:

$$R \frac{dQ}{dt} = V = -\frac{1}{C(\alpha)} \times Q + V_{oc}(\alpha) \quad (9)$$

This differential equation can be solved by specifying the motion process (specified $\alpha(t)$ profile) and the boundary condition. We chose a constant angle velocity rotation for the motion process as a typical example. The α - t relationship for constant ω is mathematically given by

$$\alpha(t) = \omega t \quad (10)$$

Since the disk structure and rotation process is periodic, output from any initial boundary condition will gradually converge to a periodic output wave with the same period after the first few periods.^[29] By applying the periodic boundary condition

$$Q(t=0) = Q\left(t = \frac{2\theta_0}{\omega}\right) \quad (11)$$

the steady-state output of metal RF-TENG for arbitrary load resistance can be calculated. This boundary condition can also be given by

$$Q_0 = Q(t=0) = \frac{N\sigma\theta_0(r_2^2 - r_1^2) - \left(-\frac{a}{b}\right)^{A_1} \int_0^{\theta_0} \frac{A_2 t}{(a-t)(t-b)} \left(\frac{a-t}{t-b}\right)^{A_1} dt}{\left(-\frac{a}{b}\right)^{2A_1} + 1} \quad (12)$$

where a , b , A_1 , and A_2 are, respectively, defined as

$$a = \frac{\theta_0}{2\omega} + \frac{1}{2} \sqrt{\frac{\theta_0^2}{\omega^2} + \frac{8d\theta_0C_p}{N\epsilon_0\epsilon_r\omega^2(r_2^2 - r_1^2)}}$$

$$b = \frac{\theta_0}{2\omega} - \frac{1}{2} \sqrt{\frac{\theta_0^2}{\omega^2} + \frac{8d\theta_0C_p}{N\epsilon_0\epsilon_r\omega^2(r_2^2 - r_1^2)}}$$

$$A_1 = -\frac{2d\theta_0}{N\epsilon_0\epsilon_r\omega^2(r_2^2 - r_1^2) \sqrt{\frac{\theta_0^2}{\omega^2} + \frac{8d\theta_0C_p}{N\epsilon_0\epsilon_r\omega^2(r_2^2 - r_1^2)}}$$

$$A_2 = \frac{2d\theta_0\sigma}{R\epsilon_0\epsilon_r\omega}$$

The equations for Q are presented as follows

$$Q = \left(\frac{a-t}{t-b}\right)^{-A_1} \left[\int_0^t \frac{A_2 t}{(a-t)(t-b)} \left(\frac{a-t}{t-b}\right)^{A_1} dt + \left(\frac{a}{-b}\right)^{A_1} Q_0 \right], \quad 0 \leq t \leq \frac{\theta_0}{\omega} \quad (13a)$$

$$Q = N\sigma\theta_0(r_2^2 - r_1^2) - \left(\frac{a-t+\theta_0/\omega}{t-\theta_0/\omega-b}\right)^{-A_1} \int_0^{t-\theta_0/\omega} \frac{A_2 t}{(a-t)(t-b)} \left(\frac{a-t}{t-b}\right)^{A_1} dt + \left[Q\left(\frac{\theta_0}{\omega}\right) - N\sigma\theta_0(r_2^2 - r_1^2) \right] \times \left(\frac{a}{-b}\right)^{A_1} \times \left(\frac{a-t+\theta_0/\omega}{t-\theta_0/\omega-b}\right)^{-A_1}, \quad \frac{\theta_0}{\omega} \leq t \leq \frac{2\theta_0}{\omega} \quad (13b)$$

Through the differentiation of Q by t , we can obtain the equations of current I for arbitrary load resistance. Then the voltage V can be calculated by the Ohm's law. For a more detailed derivation, see the Supporting Information, Section 4.1.

We calculated the profiles of Q , I , and V at different loads for $N = 4$ and $\omega = 20\pi$ rad s⁻¹ utilizing the analytical model, as shown in **Figure 4a-c**. The calculated parameters were set the same as shown in Table 1, and the C_p adopted the FEM data for a very small θ_g/θ_0 ratio of 1/89. The outputs at any resistance load are periodic waves, and the results only in one cycle are presented. When the load resistance R is less than 1 M Ω , the curves of Q , I , and V are similar to the SC curve that is given by Equation (5). The charge curve is nearly linear, and the current curve is close to a square wave. The voltage is essentially zero due to the low resistance of charge transport. As the resistance R increases, the oscillation magnitude of the charge curve decreases gradually, because the charge transport becomes more limited. The voltage curve converges toward the OC curve with an increasing positive peak value. It should be noted that the V at infinitely large resistance is the real open-circuit voltage. The positive peak value of current increases first, ascribed to the greater increasing speed of voltage peak value than that of resistance, and then drops to 0. When the load resistance is sufficiently high, very few charges can transfer leading to nearly zero charge and zero current. An important feature of the curves of I and V is that the integration of the AC signals in the entire period is zero,

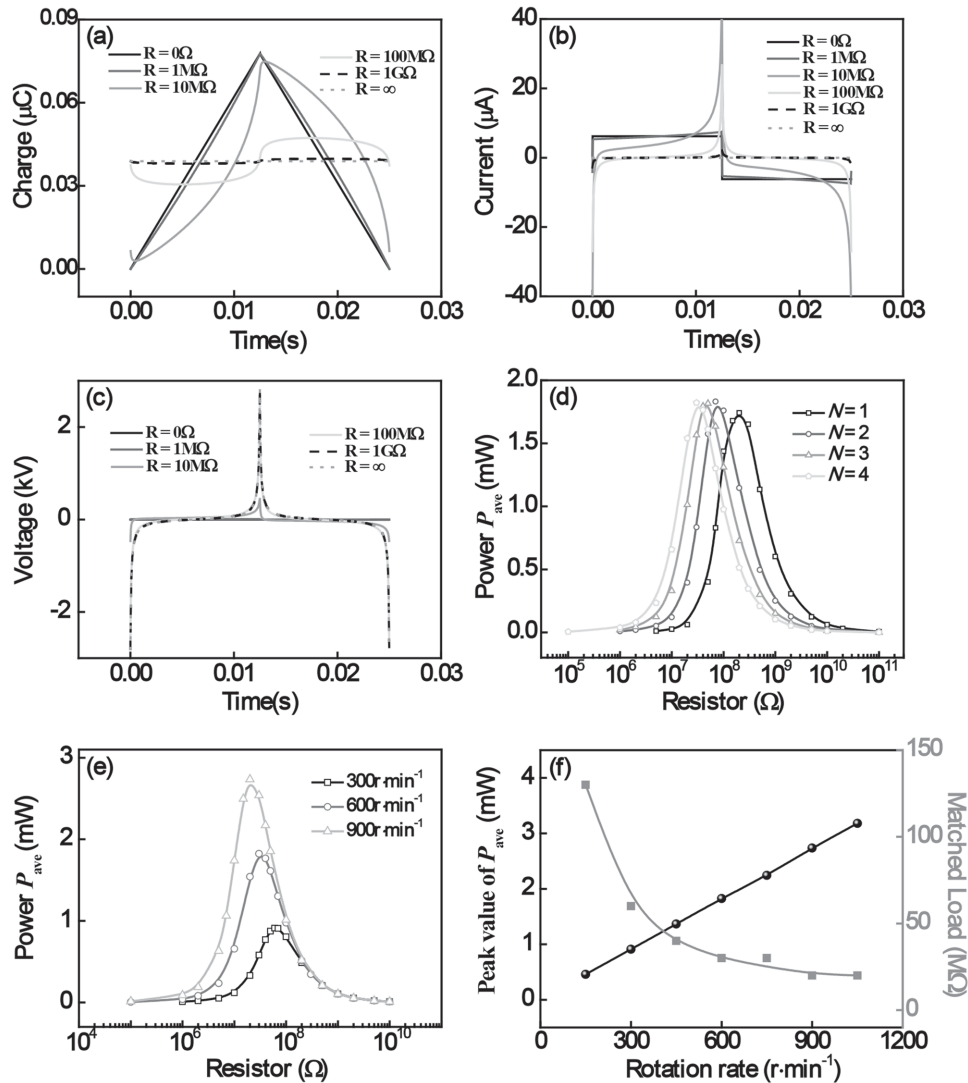


Figure 4. Output characteristics for metal RF-TENG during one cycle with grating number $N = 4$: a) transferred charge–time relationship at different load resistances, b) current–time relationship at different load resistances, and c) voltage–time relationship at different load resistances. d) Average power P_{ave} as a function of resistance for various grating numbers. e) P_{ave} as a function of resistance for various rotation rates. f) Dependences of P_{ave} peak and matched load on rotation rate.

which is the unique characteristics of TENGs with periodic structure.

Subsequently, the average output power P_{ave} of metal RF-TENG was calculated for various grating numbers ($\omega = 20\pi \text{ rad s}^{-1}$) and rotation rates ($N = 4$). The P_{ave} was defined by the following equation

$$P_{\text{ave}} = \frac{\int_0^T I^2 R dt}{T}, \quad T = \frac{2\theta_0}{\omega} \quad (14)$$

The numerical results are shown in Figure 4d–f. For the influence of N , a finer pitch can generate higher output power in the low resistance range, where the power is mainly dominated by I_{SC} . However, a wider pitch can generate higher output

power in the high resistance range, where the generated power is mainly determined by V_{OC} . The optimum resistance (the resistance at which the P_{ave} is maximized) shifts significantly to lower values with increasing the N due to the higher I_{SC} and lower V_{OC} (Figure 3b,d). The underlying reason is that the grating number has a great influence on the inherent capacitance of TENG, and thereby manipulates the impedance match between the C and load resistance. Considering the peak value of P_{ave} (optimum power, in Figure 4d), a finer pitch does not significantly improve the power output, since the V_{OC} decreases more markedly than I_{SC} increases in the low N range. On the other hand, when the rotation rate increases, the optimum resistance decreases, but the peak value of P_{ave} increases linearly (Figure 4e,f). The trend of optimum resistance can further validate the availability of impedance expression of $1/\omega C$ for a TENG.

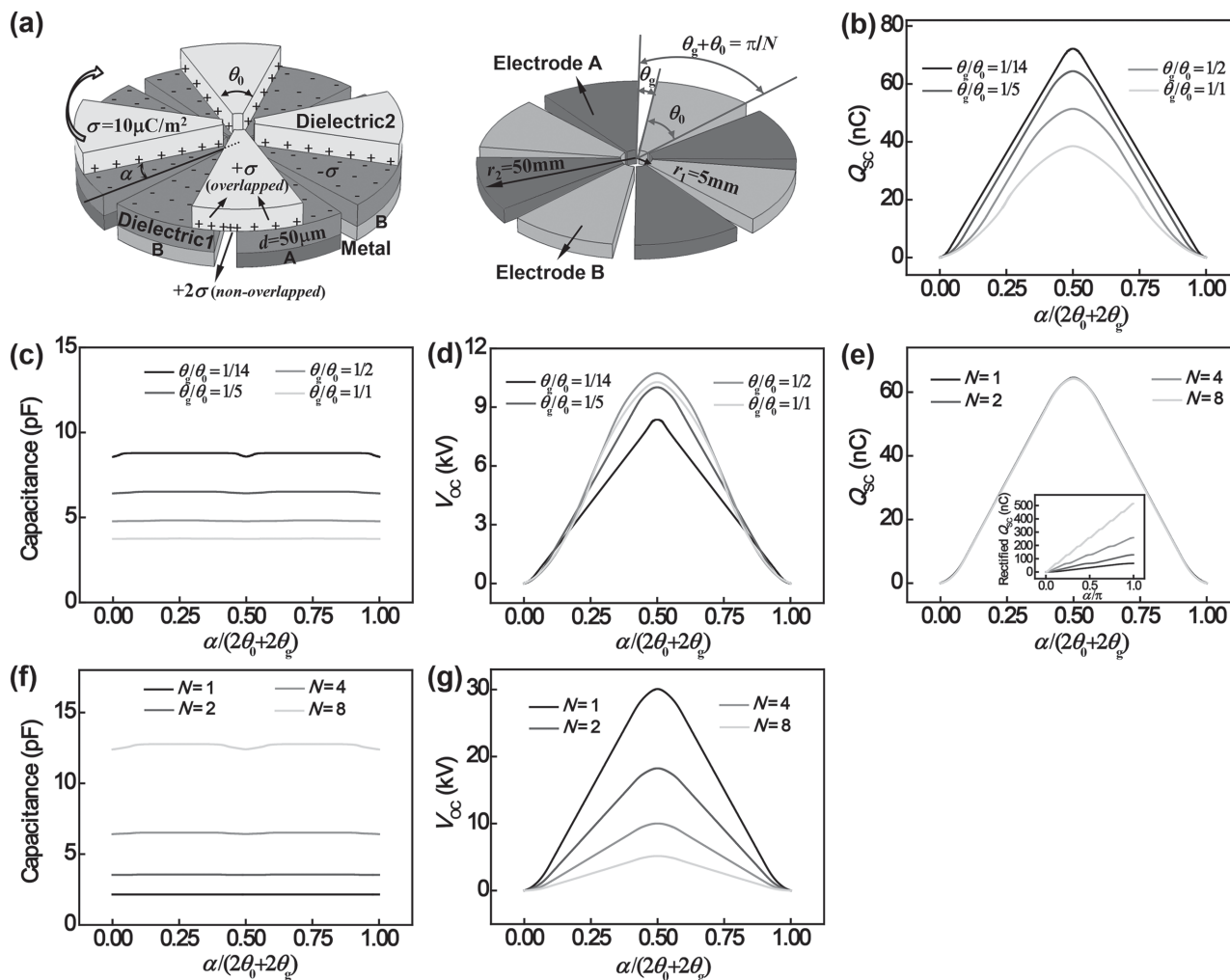


Figure 5. a) FEM model of dielectric rotary freestanding TENG. b) Short-circuit charge Q_{SC} , c) capacitance C , and d) open-circuit voltage V_{OC} of dielectric RF-TENG with $N = 4$ during one cycle for various θ_g/θ_0 ratios under the reference state. e–g) Q_{SC} , C , and V_{OC} of the dielectric RF-TENG with $\theta_g/\theta_0 = 1/5$ during one full cycle for various N .

3. Dielectric-to-Dielectric Rotary Freestanding TENG

Besides the conductor-to-dielectric RF-TENG, we also studied the basic properties and load output performance of dielectric-to-dielectric type of RF-TENG (dielectric RF-TENG). Its FEM model was constructed and shown in **Figure 5a**, and the only geometrical structure difference is that the freestanding metal layer is displaced by another dielectric layer. The dielectrics on top of electrodes and freestanding dielectrics with the same thickness of d ($50 \mu\text{m}$) are denoted by Dielectrics 1 and 2, whose relative permittivities were chosen as $\epsilon_{r1} = 3$ and $\epsilon_{r2} = 5$. Since Dielectric 1 is more triboelectrically negative than Dielectric 2, there are net positive electrostatic charges generated on surface of Dielectric 2 and net negative electrostatic charges on surface of Dielectric 1. Under SC and OC conditions, the charge density of the lower face of Dielectric 2 was assigned as $+\sigma$ in the overlapped region with Dielectric 1 and $+2\sigma$ in the non-overlapped region, and other boundary conditions are the same as the metal RF-TENG.

The Q_{SC} , C , and V_{OC} for the dielectric RF-TENG as functions of gap/unit ratio θ_g/θ_0 and grating number N were numerically

calculated and plotted in **Figure 5b–g**. Similar to the metal RF-TENG, as the θ_g/θ_0 increases, the Q_{SC-max} and C both decrease, but V_{OC-max} first rises and then drops (**Figure 5b–d**). Different from the metal RF-TENG, the constant regions of Q_{SC} at two ends of one half-cycle disappear for the dielectric RF-TENG because the charges on the dielectric surface cannot move freely. The I_{SC} also has a large difference (**Figure S8**, Supporting Information). The C profiles of dielectric RF-TENG are nearly constant due to the absence of metal screening effect when the freestanding layer rotates. As a result, the V_{OC} has the same profile shape as the Q_{SC} (without a sharp change). On the other hand, the grating number N does not influence the Q_{SC} in each cycle but can increase the accumulated charge and I_{SC} (**Figure 5e** and **Figure S8b**, Supporting Information). The increase of capacitance with increasing N leads to the decrease of V_{OC} (**Figure 5f–g**).

Then we also studied the resistive output characteristics for the dielectric RF-TENG under ideal conditions. The equation of Q_{SC} at a low N when neglecting the electrode gap is the same as that of metal RF-TENG (Equation (5)), but the capacitance C

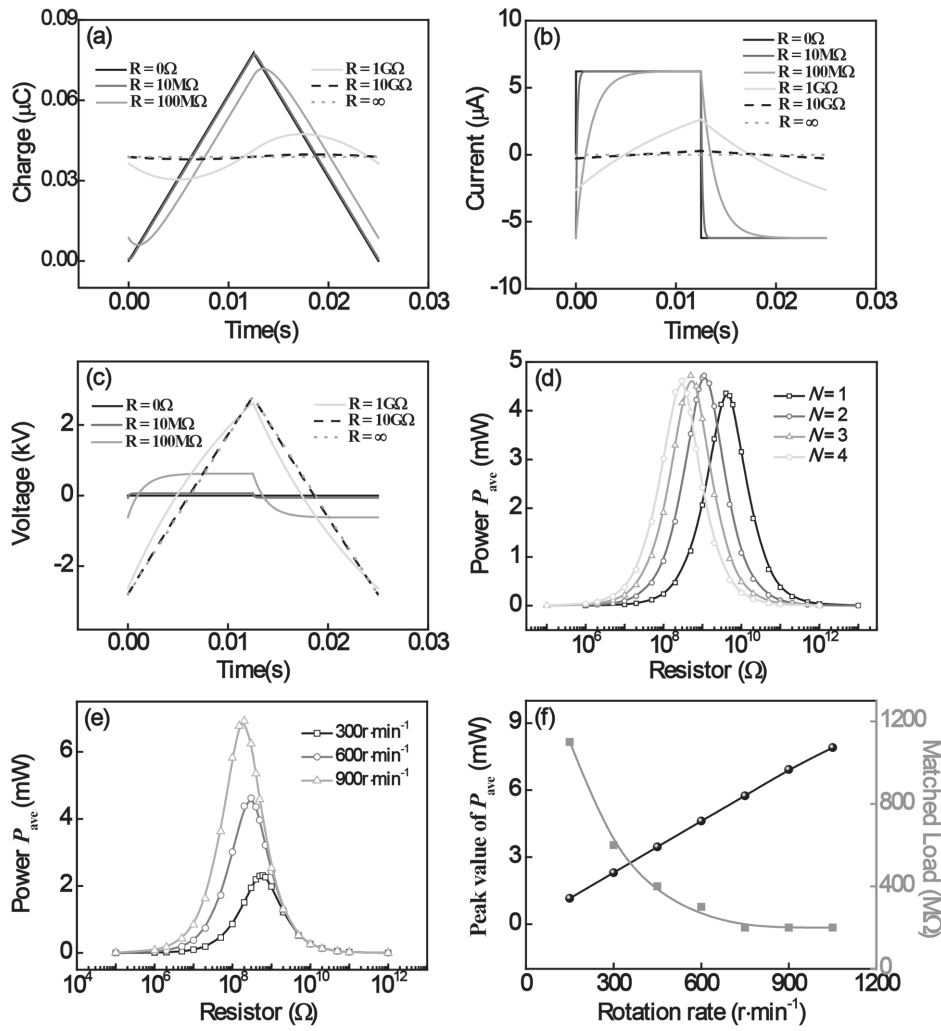


Figure 6. Output characteristics for dielectric RF-TENG during one cycle with grating number $N = 4$: a) transferred charge–time relationship at different load resistances, b) current–time relationship at different load resistances, and c) voltage–time relationship at different load resistances. d) Average power P_{ave} as a function of resistance for various grating numbers. e) P_{ave} as a function of resistance for various rotation rates. f) Dependences of P_{ave} peak and matched load on rotation rate.

approximately equals the C_p between electrodes constantly. So the governing equation is relatively simple, given by

$$V = \begin{cases} -\frac{1}{C_p}Q + \frac{N\sigma\alpha(r_2^2 - r_1^2)}{C_p} & 0 \leq \alpha \leq \theta_0 \\ -\frac{1}{C_p}Q + \frac{N\sigma(2\theta_0 - \alpha)(r_2^2 - r_1^2)}{C_p} & \theta_0 \leq \alpha \leq 2\theta_0 \end{cases} \quad (15)$$

By applying above-mentioned periodic boundary condition, which can also be given by

$$Q_0 = \frac{1 - \exp\left(-\frac{\theta_0}{\omega RC_p}\right)}{1 + \exp\left(-\frac{\theta_0}{\omega RC_p}\right)} N\sigma\omega RC_p (r_2^2 - r_1^2) \quad (16)$$

we obtain the Q – t relationship equation as follows

$$Q = N\sigma(r_2^2 - r_1^2)(\omega t - \omega RC_p) + [Q_0 + N\sigma\omega RC_p(r_2^2 - r_1^2)] \exp\left(-\frac{t}{RC_p}\right), \quad (17a)$$

$$0 \leq t \leq \frac{\theta_0}{\omega}$$

$$Q = N\sigma(r_2^2 - r_1^2)(2\theta_0 - \omega t + \omega RC_p) + \left[Q\left(\frac{\theta_0}{\omega}\right) - N\sigma(r_2^2 - r_1^2)(\theta_0 + \omega RC_p)\right] \exp\left(-\frac{\omega t - \theta_0}{\omega RC_p}\right), \quad (17b)$$

$$\frac{\theta_0}{\omega} \leq t \leq \frac{2\theta_0}{\omega}$$

For a detailed derivation, see the Supporting Information, Section 4.2.

The real-time output characteristics of dielectric RF-TENG, i.e., $Q-t$, $I-t$, and $V-t$ relationships, were calculated as shown in Figure 6a–c. The trend of Q with the resistance R is similar to that of metal RF-TENG. However, for these I and V curves, there exists some differences with the metal RF-TENG. The maximum current at a load resistance cannot exceed the SC current (Figure 6b), and the voltage curve is nearly linear close to the OC curve when the load resistance is sufficiently high (Figure 6c). The linearity of voltage at infinitely large resistance is due to the constant capacitance and linear Q_{SC} . In addition, the dielectric RF-TENG delivers the optimum power at a lower optimum resistance for a larger N which is dependent of the capacitance (Figure 6d). Meanwhile, the optimum resistance decreases with increasing the rotation rate, but the optimum power increases linearly (Figure 6e,f). Through a comparison, we can find that the dielectric RF-TENG generates higher average output power at a higher optimum resistance relative to the metal RF-TENG, which may serve as important guidance for rational design of TENG structure in specific applications. The higher optimum resistance of dielectric RF-TENG is because of its smaller capacitance, which is time-invariant and nearly equal to the parasitic capacitance C_p between electrodes. The capacitance for metal RF-TENG is the combination of two parts, i.e., C_p and serial connection of C_A and C_B , which is induced by the screening effect of metal rotator. Although this capacitance is time-variant due to the position changing of metal rotator, the average capacitance is still much larger than the C_p in the dielectric RF-TENG case. The detailed results can be seen in Figures 2b and 3c. The optimum resistance can be thought as the “impedance” match between C and the load resistance, therefore, the smaller average capacitance elevates the optimum resistance of dielectric RF-TENG.

4. Conclusions

In this work, a theoretical model was built for the grating-structured RF-TENG, including the metal RF-TENG and dielectric RF-TENG. The FEM simulations were first carried out to characterize the basic properties of RF-TENG. The Q_{SC} , C , and V_{OC} were found to be controlled by the structural parameters of TENG, i.e., the electrode gap and grating number. Based on the FEM results, approximate analytical equations were derived for two types of RF-TENG under ideal conditions. Then the dynamic output performance of TENG at arbitrary load resistance was calculated. Finally, the dependencies of optimum output power and optimum resistance on the structural parameters and rotation rate were demonstrated. The results gained from this work provide useful theoretical information for further improvement of the RF-TENG in energy harvesting and self-powered system applications.

Supporting Information

Supporting Information is available from the Wiley Online Library or from the author.

Acknowledgements

T.J. and X.C. contributed equally to this work. Support from the “thousands talents” program for the pioneer researcher and his innovation team, China, and the Beijing Municipal Science & Technology Commission (Z131100006013004, Z131100006013005) are appreciated.

Received: February 2, 2015

Revised: March 13, 2015

Published online:

- [1] E. P. Murray, T. Tsai, S. A. Barnett, *Nature* **1999**, *400*, 649.
- [2] Z. L. Wang, *Adv. Mater.* **2012**, *24*, 280.
- [3] S. H. Wang, L. Lin, Z. L. Wang, *Nano Energy* **2015**, *11*, 436.
- [4] Z. L. Wang, J. H. Song, *Science* **2006**, *312*, 242.
- [5] Y. Qin, X. D. Wang, Z. L. Wang, *Nature* **2008**, *451*, 809.
- [6] P. Basset, D. Galayko, A. M. Paracha, F. Marty, A. Dudka, T. Bourouina, *J. Micromech. Microeng.* **2009**, *19*, 115025.
- [7] D. Kraemer, B. Poudel, H. P. Feng, J. C. Caylor, B. Yu, X. Yan, Y. Ma, X. Wang, D. Wang, A. Muto, K. McEnaney, M. Chiesa, Z. Ren, G. Chen, *Nat. Mater.* **2011**, *10*, 532.
- [8] F. R. Fan, Z. Q. Tian, Z. L. Wang, *Nano Energy* **2012**, *1*, 328.
- [9] Y. Yang, H. L. Zhang, J. Chen, Q. S. Jing, Y. S. Zhou, X. N. Wen, Z. L. Wang, *ACS Nano* **2013**, *7*, 7342.
- [10] C. Zhang, T. Zhou, W. Tang, C. B. Han, L. M. Zhang, Z. L. Wang, *Adv. Energy Mater.* **2014**, *4*, 1301798.
- [11] Y. J. Su, X. N. Wen, G. Zhu, J. Yang, J. Chen, P. Bai, Z. M. Wu, Y. D. Jiang, Z. L. Wang, *Nano Energy* **2014**, *9*, 186.
- [12] G. Zhu, Y. S. Zhou, P. Bai, X. S. Meng, Q. S. Jing, J. Chen, Z. L. Wang, *Adv. Mater.* **2014**, *26*, 3788.
- [13] S. M. Niu, Y. S. Zhou, S. H. Wang, Y. Liu, L. Lin, Y. Bando, Z. L. Wang, *Nano Energy* **2014**, *8*, 150.
- [14] C. Zhang, W. Tang, C. B. Han, F. R. Fan, Z. L. Wang, *Adv. Mater.* **2014**, *26*, 3580.
- [15] Z. L. Wang, *ACS Nano* **2013**, *7*, 9533.
- [16] C. B. Han, W. M. Du, C. Zhang, W. Tang, L. M. Zhang, Z. L. Wang, *Nano Energy* **2014**, *6*, 59.
- [17] S. H. Wang, L. Lin, Y. N. Xie, Q. S. Jing, S. M. Niu, Z. L. Wang, *Nano Lett.* **2013**, *13*, 2226.
- [18] F. R. Fan, L. Lin, G. Zhu, W. Z. Wu, R. Zhang, Z. L. Wang, *Nano Lett.* **2012**, *12*, 3109.
- [19] S. M. Niu, S. H. Wang, L. Lin, Y. Liu, Y. S. Zhou, Y. F. Hu, Z. L. Wang, *Energy Environ. Sci.* **2013**, *6*, 3576.
- [20] S. H. Wang, Y. N. Xie, S. M. Niu, L. Lin, Z. L. Wang, *Adv. Mater.* **2014**, *26*, 2818.
- [21] Y. N. Xie, S. H. Wang, S. M. Niu, L. Lin, J. Yang, Z. Y. Wu, Z. L. Wang, *Adv. Mater.* **2014**, *26*, 6599.
- [22] W. Tang, C. B. Han, C. Zhang, Z. L. Wang, *Nano Energy* **2014**, *9*, 121.
- [23] G. Zhu, J. Chen, T. J. Zhang, Q. S. Jing, Z. L. Wang, *Nat. Commun.* **2014**, *5*, 3426.
- [24] C. B. Han, C. Zhang, W. Tang, X. H. Li, Z. L. Wang, *Nano Res.* **2014**, DOI: 10.1007/s12274-014-0555-3.
- [25] W. Tang, Y. Han, C. B. Han, C. Z. Gao, X. Cao, Z. L. Wang, *Adv. Mater.* **2015**, *27*, 272.

- [26] L. Lin, S. H. Wang, S. M. Niu, C. Liu, Y. N. Xie, Z. L. Wang, *ACS Appl. Mater. Interfaces* **2014**, *6*, 3031.
- [27] Y. S. Zhou, Y. Liu, G. Zhu, Z. H. Lin, C. F. Pan, Q. S. Jing, Z. L. Wang, *Nano Lett.* **2013**, *13*, 2771.
- [28] H. T. Baytekin, A. Z. Patashinski, M. Branicki, B. Baytekin, S. Soh, B. A. Grzybowski, *Science* **2011**, *333*, 308.
- [29] S. M. Niu, S. H. Wang, Y. Liu, Y. S. Zhou, L. Lin, Y. F. Hu, K. C. Pradel, Z. L. Wang, *Energy Environ. Sci.* **2014**, *7*, 2339.
- [30] S. M. Niu, Y. Liu, S. H. Wang, L. Lin, Y. S. Zhou, Y. F. Hu, Z. L. Wang, *Adv. Mater.* **2013**, *25*, 6184.
- [31] S. M. Niu, Y. Liu, S. H. Wang, L. Lin, Y. S. Zhou, Y. F. Hu, Z. L. Wang, *Adv. Funct. Mater.* **2014**, *24*, 3332.
-